Asymmetrical Functionalization of Polarizable Interface Restructuring Molecules for Rapid and Longer Operative Lithium Metal Batteries

Chae Yeong Son, Daehyun Kim, Seo-Young Jun, Haesun Park,* and Won-Hee Ryu*

Lithium metal batteries (LMBs) have been recognized as high-energy storage alternatives; however, problematic surface reactions due to dendritic Li growth are major obstacles to their widespread utilization. Herein, a 3-mercapto-1-propanesulfonic acid sodium salt (MPS) with asymmetrically functionalized thiol and sulfonate groups as polarizable interface-restructuring molecules is proposed to achieve rapid and longer-operating LMBs. Under a harsh condition of 5 mA cm^{-2}, Li–Li symmetric cells employing MPS can be cycled over 1200 cycles, outperforming those employing other molecules symmetrically functionalized by thiol or sulfonate groups. The improved performance of the Li|V$_2$O$_5$ full cell is demonstrated by introducing MPS additives. MPS additives offer advantages by flattening the surface, reconfiguring Li nucleation and growth along the stable (110) plane, and forming a durable and conductive solid–electrolyte interface layer (SEI). This study suggests an effective way to develop a new class of electrolyte additives for LMBs by controlling engineering factors, such as functional groups and polarizable properties.

1. Introduction

Rechargeable energy storage technology has been revolutionized by the development of lithium-ion batteries (LIBs), comprising transition metal-based oxide cathodes and carbonaceous graphite anodes.[1] Nevertheless, the increasing demand for long-lasting batteries has pushed researchers to modify existing electrode materials to achieve higher energy densities.[2] Lithium-metal batteries (LMBs) using Li-metal anodes (e.g., Li–S and Li–air

batteries) are promising candidates for high-energy next-generation batteries because of their exceptional merits, offering the highest theoretical specific capacity (3860 mAh g^{-1}), the lowest redox potential (−3.04 V vs SHE), and low gravimetric densities (0.534 g cm^{-3}).[3] However, the random directional formation of Li dendrites owing to nonuniform deposition often compromises battery safety requirements.[4] Pieces of dendrites accidently detached from the surface get converted to dead Li, thereby degrading the coulombic efficiency.[5] In addition, an unstable and fragile solid-electrolyte interphase (SEI) layer, which spontaneously forms at the interface between Li and the electrolyte, can lead to issues related to electrolyte depletion and unwanted surface passivation, causing continuous capacity retention during cycling.[6]

Substantial efforts have been undertaken to address the unstable and problematic surface reactions on Li anodes by introducing effective strategies, such as utilizing 3D current collector hosts,[7] modifying electrolyte components,[8] designing separators,[9] regulating Li-ion flux,[10] and introducing functional electrolyte additives.[11] Among these, incorporating electrolyte additives has been considered to reform the SEI layer species via the self-reduction of additive molecules because their lowest unoccupied molecular orbital (LUMO) levels are lower than those of the electrolyte species.[12] In addition to the SEI modification function, the random growth phenomena of Li dendrites should be controlled to further stabilize the problematic surface reaction of Li metal and prevent the short-circuit issues of LMBs.[13]

Considering the reduction chemistry of Li$^+$ ions to Li metal deposited on the surface, conventional electroplating technologies, such as copper plating, can provide useful insights for controlling electrodeposited surface morphologies by the addition of functional additives. Electroplating requires achieving a uniformity on copper surfaces.[14] During copper plating processes, copper ions tend to unevenly adsorb and irregularly nucleate on substrate surfaces owing to inhomogeneous surface features or high current density conditions, resulting in valley structures with abrupt height variations compared to the surroundings called "dendrites." To address this issue, a class of functional additives, such as 3-Mercapto-1-propanesulfonic acid sodium salt (MPS),

C. Y. Son, S.-Y. Jun, W.-H. Ryu
Department of Chemical and Biological Engineering
Sookmyung Women's University
100 Cheongpa-ro 47-gil, Yongsan-gu, Seoul 04310, Republic of Korea
E-mail: whryu@sookmyung.ac.kr
D. Kim, H. Park
School of Integrative Engineering
Chung-Ang University
84 Heukseok-ro, Dongjak-gu, Seoul 06974, Repubilc of Korea
E-mail: parkh@cau.ac.kr
W.-H. Ryu
Institute of Advanced Materials and Systems
Sookmyung Women's University
100 Cheongpa-ro 47-gil, Yongsan-gu, Seoul 04310, Republic of Korea

(iD) The ORCID identification number(s) for the author(s) of this article can be found under https://doi.org/10.1002/smll.202405143
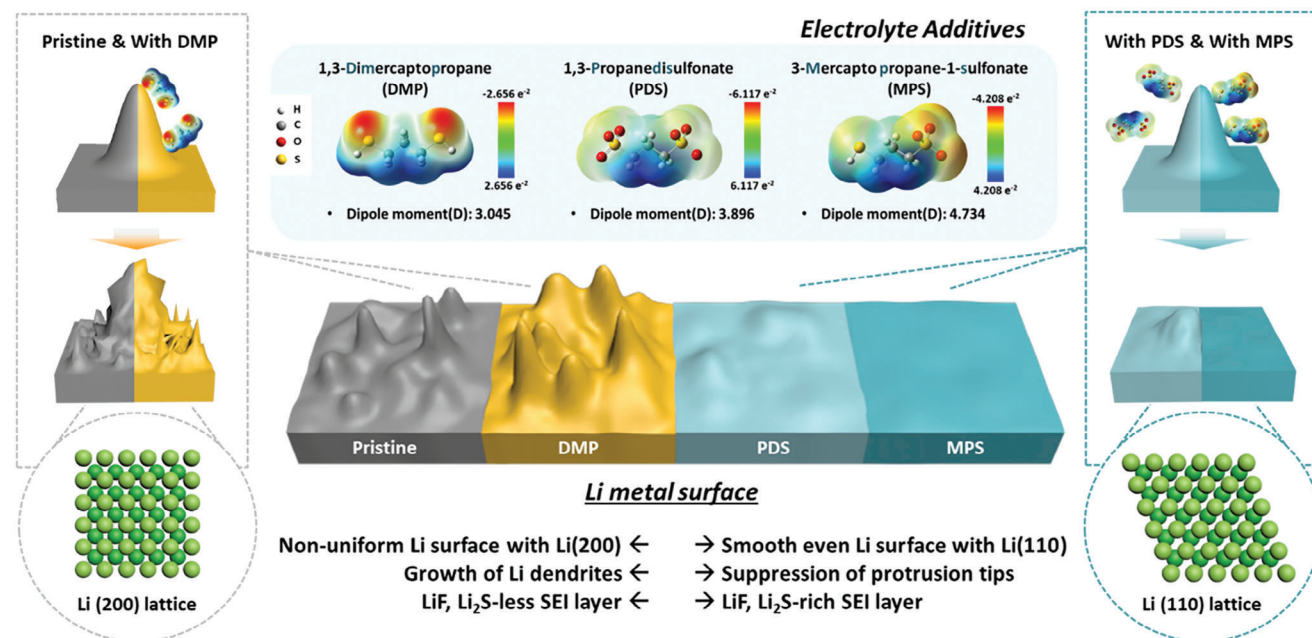
Figure 1. Schematic illustration of the crystalline rearrangement and surface flattening effects of various electrolyte additives (DMP, PDS, and MPS) with symmetric and asymmetric thiol and sulfonate functional groups on Li metal anodes.

can serve as plating accelerators (called brighteners), and play a crucial role in filling the defects and low-height empty spaces by expediting charge diffusion.[15] These accelerators can preferentially accumulate metal deposits within grooves on the metal surface. Therefore, the introduction of an accelerator additive is expected to contribute to the creation of defect-free and homogeneous metal surfaces that function as surface-leveling or flattening agents.[16]

Inspired by identical electroplating additive technologies, utilizing the accelerator additive in Li metal plating in batteries can be an alternative solution to make meaningful progress in intentionally regulating the Li deposition behavior to obtain smooth and flat surfaces. In this study, we introduce MPS into the electrolyte as an accelerating additive, to stabilize the surface reaction chemistry of Li metal anodes for realizing long-lifespan Li metal batteries. MPS comprises a propane backbone with asymmetric thiol and sulfonate functional groups. To elucidate the effect of each thiol and sulfonate functional group and control the geometric dipole moment, we investigated reference molecules for comparison with MPS molecules, such as i) 1,3-dimercapto propane (DMP) composed of symmetric thiol groups and ii) propane-1,3-disulfonic acid disodium salt (PDS) composed of symmetric sulfonate groups. Polar functional groups in MPS was expected to facilitate a homogenous Li-ion flux and consequently, smooth Li deposition.[8a] As illustrated in **Figure 1**, an MPS molecule electrolyte additive with a high dipole moment offers the following advantages: i) inhibition of Li dendrite growth under harsh conditions over long-term cycling, ii) crystalline rearrangement of the Li metal structure for homogeneous deposition, and iii) formation of high-quality SEI layers with durable LiF and ion-conductive Li_2S components. Electrochemical tests were conducted using the additive molecules to verify their beneficial functions. The morphological and structural characteris-

tics of the Li metal cycled with different molecular additives were examined. To better understand the Li plating reaction mechanism with the additives, we performed density functional theory (DFT) calculations to compare the binding energy changes of Li at possible nucleation sites, such as concave and convex sites, on the Li metal at the surface. Our research strategy provides a new perspective and an effective pathway for the development of effective electrolyte additives for high-performance and safe LMBs.

2. Results and Discussions

2.1. Electrochemical Performance of Li–Li Symmetric Cells Employing DMP, PDS, and MPS

We introduced MPS, known as an accelerating and brightening electroplating additive, and further manipulated the polyanion functional groups at either end of the propane backbone using thiol- and sulfonate-terminated groups (Figure 1). DMP and PDS have symmetric functional groups based on the thiol or sulfonate ends, respectively. In contrast, MPS consists of asymmetric functional groups with thiol and sulfonate groups. To verify the surface stabilizing effects of the DMP, PDS, and MPS additives on the electrochemical performance, cycling performance tests were conducted with Li–Li symmetric cells at current densities of 1 and 5 mA cm^{-2} (**Figures 2**a–d and S1, Supporting Information). As shown in the voltage-time profiles in Figure 2a and Figure S1a (Supporting Information), at a low current density of 1 mA cm^{-2}, the Li–Li cell without the additive maintained a voltage of ≈80 mV for the initial cycles. However, it exhibited a sudden increase in overpotential after 172 h and significant polarizations up to ± 1 V after 206 h. In the case of DMP, a relatively higher initial voltage of ≈90 mV was observed, and a sudden
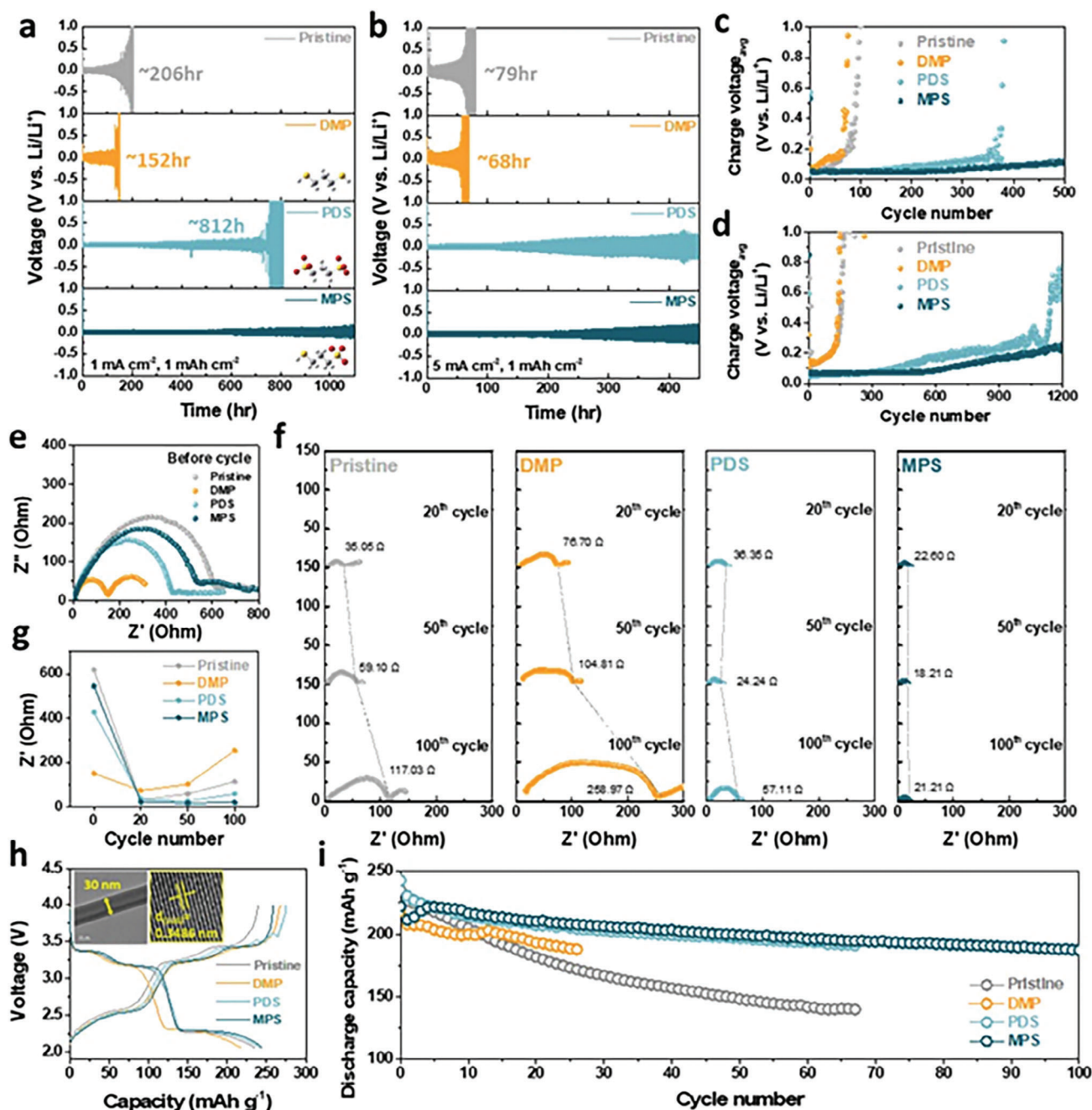
**ADVANCED
SCIENCE NEWS**

www.advancedsciencenews.com

NANO · MICRO
small

www.small-journal.com

Figure 2. Electrochemical data of cells containing electrolyte prepared without (pristine) and with DMP, PDS, and MPS additives: Cycling performance of Li–Li symmetric cells performed at a) 1 mA cm^{-2} and b) 5 mA cm^{-2} depicted as the charge/discharge curve. Cycling performance of Li–Li symmetric cells illustrated through the average charge voltage at c) 1 mA cm^{-2} and d) 5 mA cm^{-2}. EIS spectra obtained from Li–Li symmetric cells prepared without (pristine) and with DMP, PDS, and MPS additives: e) before cycle, f) after the 20th, 50th, and 100th cycle, g) resistance value with respect to the cycle number. Electrochemical performance of Li|V$_2$O$_5$ batteries without and with DMP, PDS, MPS additives: h) 2nd charge/discharge curves of the full cells with different additives (inset: SEM and TEM images of the V$_2$O$_5$ nanorod cathode material) and i) cycle performance of the full cells with different additives.

voltage rise was subsequently observed after 133 h, indicating cell deterioration compared with the pristine cell. The Li–Li symmetric cells, including that utilizing PDS, demonstrated significantly improved cycling performance for up to 500 h. The overpotential was ≈50 mV during the initial cycle and 90 mV after 500 h

(Figure S1b, Supporting Information). The MPS-containing Li–Li cells showed outstanding cycling stability throughout cycling. Furthermore, these cells showed the lowest overpotential value (≈50 mV) even after long cycling for 1100 h, verifying the best performance of the MPS additive among other cells. This

**ADVANCED
SCIENCE NEWS**

www.advancedsciencenews.com

NANO · MICRO

small

www.small-journal.com

surface leveling effect of MPS was more apparent as the current density increased to 5 mA cm^{-2}. Cycling under higher current density conditions corresponding to rapid operation causes i) frequent and severe growth of pronounced protrusions and ii) unwanted formation of the thicker and unstable SEI layers, resulting in higher voltage oscillations and faster electrolyte depletion. As observed in Figure 2b and Figure S1c (Supporting Information), Li–Li symmetric cells both using the pristine electrolyte and DMP-containing electrolyte exhibited highly irregular voltage hysteresis even from the initial cycles and experienced a sudden short-circuit before 90 h. These results imply that DMP does not function properly as an interface stabilizer. Although the PDS cells initially displayed stable cycling with low overpotentials (≈70 mV), they showed a gradual increase in overpotential after 100 h, resulting in unstable voltage polarization, even after 200 h (Figure S1d, Supporting Information). In contrast, cells using MPS maintained stable cycling with an average voltage of 70 mV and cycled reliably for over 400 h. The average charge voltage values for cycling at different current densities are shown in Figure 2c,d. The charge voltage values of the cells employing MPS at both current densities showed the lowest trend compared to the other cells. To further verify the significant stabilizing effect of MPS, Li–Li symmetric cell tests were conducted with a high capacity limit of 5 mAh cm^{-2}, at a high current density of 10 mA cm^{-2} (Figure S2, Supporting Information). The cells with MPS exhibited good cycle performance over 100 h under extremely harsh conditions, such as fast charging and high-capacity performance. We demonstrated that MPS functions as an exceptional surface planarizer with outstanding cycling performance even under rapid operating conditions. For optimization, we compared the cycle stability during Li stacking and stripping at various MPS concentrations (Figure S3, Supporting Information). We added MPS at concentrations of 0.02, 0.1, and 1 wt% (almost saturated) to the electrolyte and conducted Li–Li symmetric cell experiments under a current density and capacity of 1 mA cm^{-2} and 1 mAh cm^{-2}, respectively. The results demonstrated that higher concentrations of MPS allowed the Li–Li cells to operate for longer durations.

To investigate the charge-transfer kinetics of the various cells at different cycles, electrochemical impedance spectroscopy (EIS) measurements were conducted on the Li–Li symmetric cells before cycling and after the 20th, 50th, and 100th cycles, as shown in Figure 2e,f, and Figure S4 (Supporting Information). The charge transfer resistance (R_{ct}) usually increases when side reactions, such as electrolyte decomposition, have a negative impact on Li-ion migration. Additives with high dipole moments can significantly increase the R_{ct} value via preferential adsorption onto the Li metal surface. The additives impede the charge transfer between the Li metal and electrolyte, leading to a reduction in the active surface area of the Li metal.[17] Consequently, this adsorption increases the resistance, and the extent of the adsorption behavior is related to the dipole moment of each additive. In this regard, the Li–Li symmetric cells with MPS exhibited the highest ohmic resistance prior to cycling, followed by those with PDS and DMP, reflecting the trend in the dipole moment magnitude (Figures 1 and 2e). As described in Figure 2f,g, both R_s and R_{ct} initially decreased in the overall cells and gradually increased during cycling. After the 20th cycle, the Li–Li cells without additives and those with DMP showed R_{ct} values of 35.05 and

76.70 Ω respectively, which were even larger than those of the cells with PDS (36.35 Ω) and MPS (22.60 Ω). After the 50th cycle, the R_{ct} values of the pristine and DMP-containing cells were significantly higher than those of the cells prepared with PDS and MPS. This difference became more pronounced after the 100th cycle. Furthermore, the cell employing MPS molecules consistently maintained the lowest ohmic resistance of ≈20 Ω, unlike other cells. When comparing the charge transfer resistance after cycling for each additive, Li–Li cells prepared both without additives and with DMP exhibited a significant increase in resistance as cycling progressed. In contrast, the cells with PDS and MPS maintained relatively consistent resistance values and high interfacial stability, consistent with the cycling test results (Figure 2g). These results can be attributed to the formation of unwanted side products, such as dead Li and thick SEI components, during the Li plating/stripping processes, resulting in increased resistance to charge transfer.[18] Throughout all stages, the MPS-containing cells exhibited the smallest ohmic resistance owing to their surface protection effect, leading to rapid and stable electrochemical kinetics during the Li deposition/dissolution processes.

To confirm the practical applicability of the polarizable and interface-stabilizing electrolyte additives, full-cell tests under different electrolyte conditions were carried out by introducing an Li-free V$_2$O$_5$ cathode and Li metal anode. Because infinite Li sources already exist in the Li metal anode, a Li-free V$_2$O$_5$ cathode was used for the best combination of the full cell as a discharge-first Li-metal battery alternative. We successfully synthesized 1D and uniform V$_2$O$_5$ nanorods with diameters of 30 nm using a hydrothermal method (Figures S5 and S6, Supporting Information). This nanorod features a (110) crystalline facet corresponding to a lattice fringe of 0.3486 nm, which is the preferred intercalation channel for both lithiation and delithiation processes (Figure 2h and Figure S6, Supporting Information).[19,20] The second charge–discharge profiles of the full cell collected at a current density of 30 mA g^{-1} using the orthorhombic V$_2$O$_5$ cathode showed a typical shape with distinct plateaus owing to phase transitions based on the degree of lithium-ion intercalation. Figure 2h shows these transitions occurring at voltages of 3.4, 3.2, and 2.3 V, corresponding to the phase transitions of α/ϵ, ϵ/δ, and δ/γ, respectively.[21] The Li-V$_2$O$_5$ full cells without additives and with DMP, PDS, and MPS delivered 2nd discharge capacities of 235.5, 218.4, 218.4, and 242.9, respectively, verifying that the MPS-containing cell exhibited the highest capacity (Figure 2h). Figure 2i and Figure S7 (Supporting Information) show the cycling performances of the Li-V$_2$O$_5$ full cells collected at current densities of 30 (charge) and 60 mA (discharge) g^{-1} with and without additives, respectively. The pristine cell experienced a significant decrease in discharge capacity as the cycles progressed. Low CE values from the initial cycling were displayed in the cells with DMP, dropping to below 50% after 15 cycles Furthermore, the pristine and PDS-containing cells exhibited a sharp decline in Coulombic efficiency (CE) after the 60th cycle. In contrast, the MPS-containing cell successfully maintained a consistent CE during cycling (Figure S7, Supporting Information). From various cell tests, we concluded that asymmetrically functionalized MPS molecules with thiol and sulfonate groups showed the best performance compared to other symmetric DMP and PDS molecules.
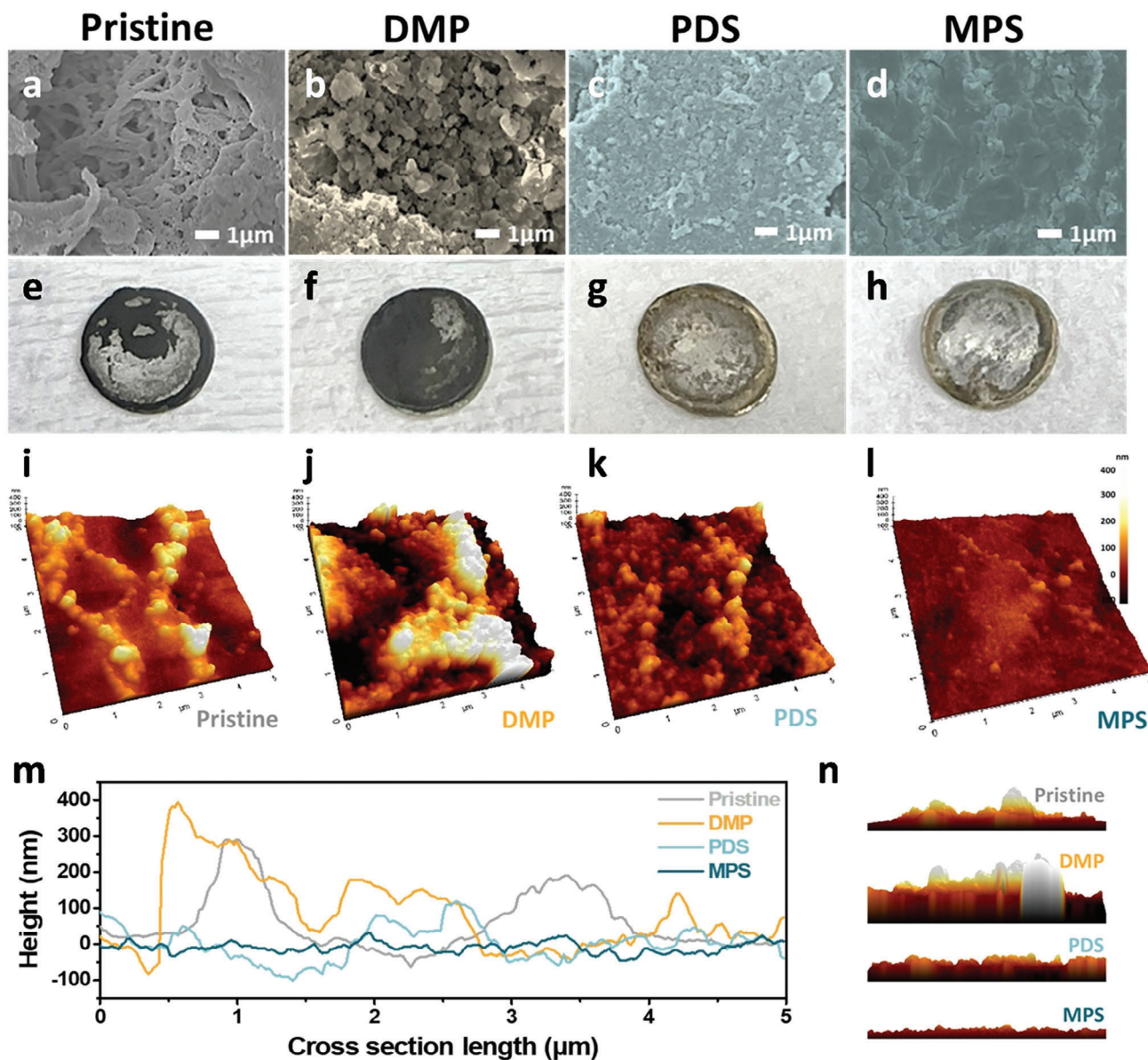
**ADVANCED
SCIENCE NEWS**

www.advancedsciencenews.com

NANO · MICRO

small

www.small-journal.com

Figure 3. Morphology of Li metal anode surface obtained from Li–Li symmetric cells: a–d) SEM images observed after 500 cycles at 5 mA cm^{-2} and 0.5 mAh cm^{-2} and e–h) digital images of the Li electrodes from Li–Li symmetric cells after cycling. i–n) AFM images of cycled Li electrodes after 100 cycles i) without additive, j) with DMP, k) with PDS, and l) with MPS. m) Cross-sectional length–height profile and n) height images from the AFM analysis.

2.2. Morphological Properties of Li Metal Surface

To directly confirm the surface flattening effects of Li metal anodes containing the DMP, PDS, or MPS electrolyte additive during cycling, ex situ surface morphological characterizations of Li metal from the corresponding Li–Li symmetric cell were investigated under a current density of 5 mA cm^{-2} with capacity of 0.5 mAh cm^{-2} after 500 cycles (**Figures 3** and S8, Supporting Information). The surface morphologies of the Li metal obtained after 500 cycles with various electrolyte additives were examined using scanning electron microscopy (SEM) (Figure 3a–d, Supporting Information). In the pristine cell, the Li metal exhibited a very rough and nonuniform surface with obvious needle-

like dendrites all over the cross-sectional images (Figure 3a and Figure S8a, Supporting Information). Dendrites originated from cracks that formed when uneven Li deposition placed a large amount of stress on the SEI layer during continuous Li charging/discharging processes.[17,22] They significantly destabilize the Li metal surface, causing a complex Li-ion flux that eventually resulted in a poor cycling performance. Similarly, highly uneven nodular features were observed in the Li metal cycled with DMP (Figure 3b and Figure S8b, Supporting Information). It was covered with numerous thick mossy dendrites and other promiscuous side-reaction products resulting from continuous plating/stripping. In contrast, the Li metal in the presence of PDS exhibited a relatively homogeneous surface with no significant

**ADVANCED
SCIENCE NEWS**

www.advancedsciencenews.com

**NANO · MICRO
small**

www.small-journal.com

debris even after cycling compared to the cycled Li electrodes without additives and with DMP; however, negligible tips and clusters of side products were present on the surface (Figure 3c and Figure S8c, Supporting Information). The surface of the Li metal containing MPS displayed the flattest and densest morphology, with no discernible tips of any kind (Figure 3d and Figure S8d, Supporting Information). The SEM results clearly correspond to the electrochemical cycle performance, as shown in Figure 2. We examined the optical appearance of the Li metal electrodes disassembled from the Li–Li symmetric cells after cycling (Figure 3e–h). As shown in Figure 3e, the blackened regions dominate the Li metal surface in the pristine cell, corresponding the undesirable byproducts. Similarly, the appearance the Li metal with DMP had most of the Li metal covered in black, with a small portion of silver remaining (Figure 3f). Conversely, it included a negligibly darkened area of Li metal disassembled from the cycled Li–Li cells with PDS (Figure 3g). In the presence of MPS, the naked Li metal also exhibited shiny silver-colored features, as on a fresh Li metal surface (Figure 3h). The electrode cycled in the presence of PDS and MPS retained characteristics similar to those of fresh Li, thereby enhancing the cycling performance of the Li metal anode. PDS and MPS molecular dipole additives with sulfonate functional groups successfully preserved the surface appearance of Li metal anodes without significant debris owing to their planarization and stabilizing effects during cycling.

Furthermore, we examined the detailed surface roughness and height deviation of the cycled Li metals with and without additives using atomic force microscopy (AFM) (Figure 3i–n). In the case of the cycled Li metal obtained from the pristine and DMP-containing cells, prominent protrusion tips with high roughness values were observed (Figure 3i,j). Both cells showed distinct height differences with obvious uneven dendrites owing to undesirable byproducts. In contrast, the Li metal cycled in the presence of PDS and MPS showed a flat Li metal surface without large dendrites. Surface uniformity is particularly evident in Figure 3k,l, where the Li metal with MPS displays almost no height variation around the baseline, while the Li metal with PDS exhibits severe height fluctuations (Figure 3m,n). The results demonstrate that the Li metal cycled with MPS can effectively maintain compact and dense Li deposition without defective porous features, which often occur owing to unstable stacking during continuous cycling. Thus, MPS surpassed other additives, even better than PDS, because of its surface flattening and stabilizing effects against problematic Li dendrite formation.

2.3. SEI Layer Composition of the Li Metal Anode after a Long Period of Time

The continuous cracking of fragile SEI layers during vigorous Li deposition and stripping exposes fresh Li to the electrolyte, leading to the continuous consumption of the electrolyte and unwanted formation of byproducts during cycling.[23] Therefore, the deliberate formation of durable SEI layers is crucial for obtaining a uniform surface structure that remains dense and crack-free even after extended cycling. Consequently, an X-ray photoelectron spectroscopy (XPS) analysis was conducted to inves-

tigate the surface and depth structures of the Li metal electrode with 0.5 mAh cm^{-2} cycled at 5 mA cm^{-2} for 500 cycles (**Figures 4a,b**, and S9, Supporting Information). In the C 1s XPS spectrum, all the samples exhibited similar C—H, C—O, CO_3^{2-}, and CF_3 peaks, corresponding to the decomposition products of the carbon-based electrolyte (Figure S9a, Supporting Information). In the Li 1s spectra obtained for the Li metal anodes cycled without additives and with DMP, peaks related to LiF, LiOH, Li_2CO_3, and Li_2O were observed along the depth (Figure S9b, Supporting Information). In contrast, the Li-metal anodes cycled with PDS and MPS exhibited enriched LiF, LiOH, Li_2CO_3, and Li_2S peaks. Similar results were observed in the O 1s spectrum (Figure S9c, Supporting Information). Peaks related to S=O, C=O, ROLi, and Li_2O phases were observed along the depth. However, for the cycled Li anodes without additives and with DMP, the Li_2O and LiOH peaks were broader and stronger, respectively, indicating the existence of an oxide-dominant SEI component. In the F 1s spectrum, the cycled Li metal anodes both without and with DMP showed low LiF peaks at 684.8 eV (Figure 4a). In contrast, the Li electrodes cycled with PDS exhibited a relatively strong LiF peak, while the electrode cycled with MPS showed the strongest LiF peak, corresponding to the electrochemical results shown in Figure 2. The presence of LiF, which is a passivation and protective component, blocks direct contact between the fresh Li metal and electrolyte, thereby preventing parasitic reactions and consequently promoting the maintenance of fresh Li.[24] In the S 2p spectrum, two distinct peaks related to lithium sulfide (e.g., Li_2S and Li_2S_2) and lithium sulfonate (e.g., $LiSO_3$ and Li_2SO_4) were observed for all samples (Figure 4b). The Li_2S content in the interfacial layer at 160.2 and 161.4 eV offer bifunctional benefits of i) high ionic conductivity ($\approx 10^{-5}$ S cm^{-1}) and ii) excellent electrical insulation properties,[25] enhancing electrode kinetics while rapidly approaching the Li metal surface to stack Li on the grooves.[26] The $LiSO_3$ and Li_2SO_4 components derived from the thiol and sulfonate functional groups of the additives reduced the resistance of the SEI layer.[27] The peak signal of the MPS case in the S 2p spectrum had the highest intensity compared to the bare reference and other additive cases. The coexistence of inorganic components based on fluorides and sulfides synergistically improves the durability and ionic conductivity of the SEI component, thus enabling enhanced cell performance. Although the cycled Li electrodes without additives and with DMP exhibited high proportions of weak and nonconductive oxide phases, such as LiOH and Li_2O, the Li metal anode cycled in the presence of PDS and MPS showed durable fluoride-rich (LiF) and conductive sulfide-rich (Li_2S) species. The advantageous combination of fluoride and sulfide components in the SEI effectively stabilized the Li metal anode during prolonged cycling. To elucidate the origin of the modified SEI component derived from symmetrically and asymmetrically functionalized additives with thiol or sulfonate groups, energy diagrams of the diverse additives and a tetraethylene glycol dimethyl ether (TEGDME) solvent, including the highest occupied molecular orbital (HOMO) and LUMO levels, are shown in Figure 4c. The HOMO levels of the additives were similar to or lower than that of TEGDME, indicating a negligible oxidation reaction on the cathode surface in the case of a full cell composed of a V_2O_5 nanorod cathode and an Li anode, as shown in Figure 2h (inset). Because we used a low upper window voltage (4 V), we could not consider the unwanted
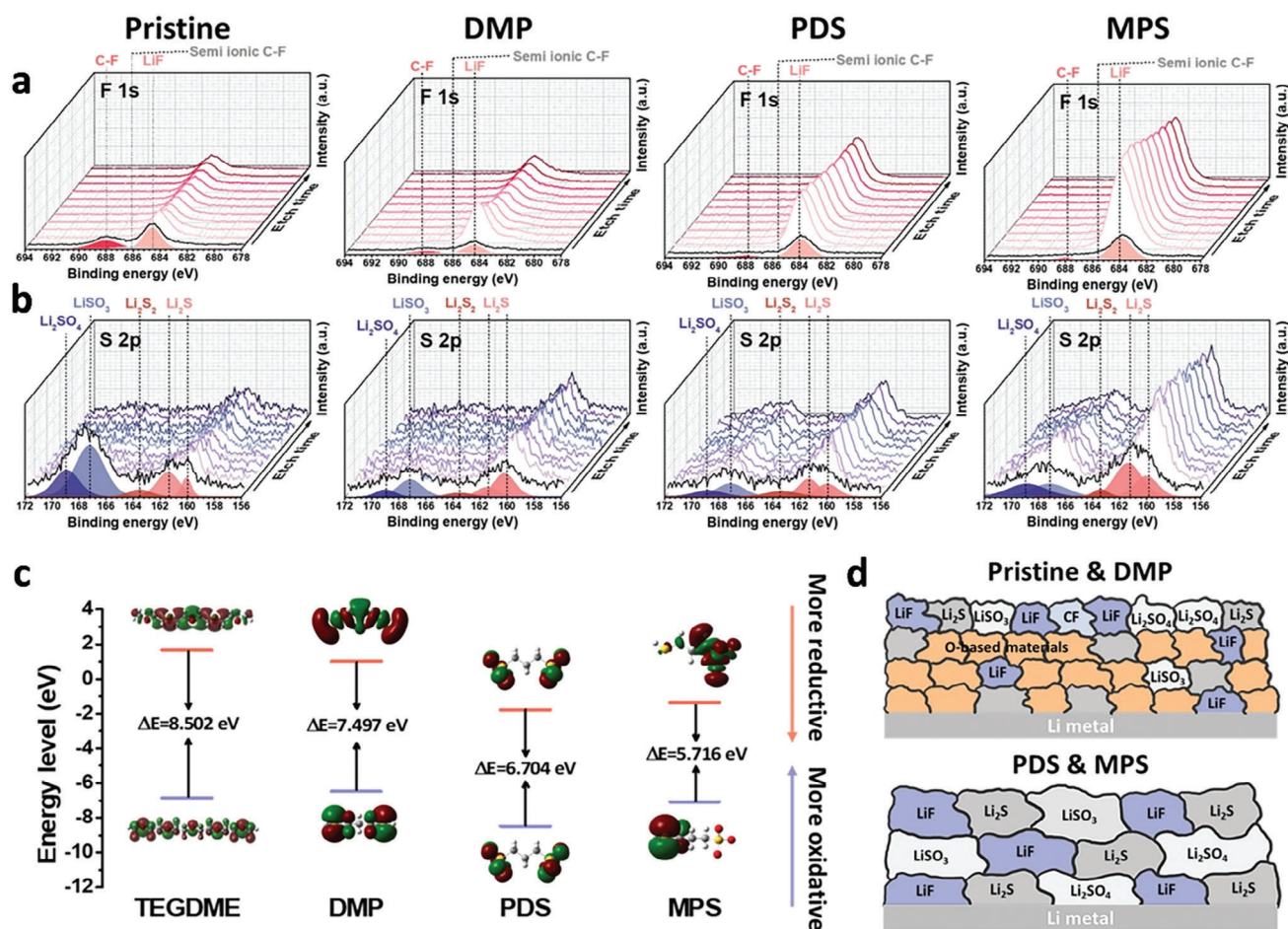
16136829, 0, Downloaded from https://onlinelibrary.wiley.com/doi/10.1002/smll.202405143 by Chung-Ang University, Wiley Online Library on [22/10/2024]. See the Terms and Conditions (https://onlinelibrary.wiley.com/terms-and-conditions) on Wiley Online Library for rules of use; OA articles are governed by the applicable Creative Commons License

ADVANCED
SCIENCE NEWS
www.advancedsciencenews.com

NANO · MICRO
small
www.small-journal.com

Figure 4. SEI layer component of the Li metal anode obtained from various Li–Li symmetric cells: XPS spectra depth profiles from the charged Li metal in an electrolyte without and with DMP, PDS, and MPS additives: a) F 1s and b) S 2p. c) Calculation data of HOMO/LUMO energy level. d) Schematic illustration showing the composition of the SEI layers formed on the surfaces of Li metal anodes.

oxidation of the additive species on the cathode surface. However, the lower LUMO level of the additives indicated more reductive characteristics compared to the TEGDME solvent, resulting in preferential decomposition and subsequent incorporation of the additive species into the SEI component prior to TEGDME. The coordination with Li ions can alter the LUMO level of both the solvent and additives. The strong electron-withdrawing effect of Li induces a reduction in electron density near the oxygen atoms in both the solvent and additives, resulting in a downward shift of the LUMO level.[28] Based on a previous report, we can expect that the LUMO of TEGDME shifts down from 1.65 to −0.35 eV,[29] which is still higher than or similar with that of PDS and MPS. Considering the further reduction of the LUMO of PDS and MPS upon coordination with Li, these additives would dominate the reduction reaction. The low LUMO energy levels of the molecular dipole additives indicate that the fluoride and sulfide species in the SEI component originate from the preferential decomposition of the additives rather than the TEGDME solvent. In the case of DMP, the LUMO level was close to that of TEGDME, resulting in an SEI component similar to that of the oxide-rich species. In contrast, the lower LUMO levels of PDS and MPS compared to those of TEGDME and DMP resulted in active decomposi-

tion and higher proportions of fluoride- and sulfide-based inorganic SEI components. To better understand the compositional differences of the Li metal anodes cycled under various conditions, a schematic illustration of the SEI components based on the XPS depth profile results is depicted in Figure 4d. The reacted Li surfaces in both the pristine and DMP-containing interfaces had various components, including fluoride and sulfide species, on the top side of the SEI layer. However, various O-rich species became dominant in the SEI layer, indicating continuous SEI-layer deterioration during the constant Li plating/stripping processes. Conversely, the interface layers of the Li metal anodes cycled with PDS and MPS consistently show homogeneous fluoride- and sulfide-based materials regardless of the depth. The SEI layer of the Li metal anodes cycled with MPS maintained the highest ratio of fluoride and sulfide, even when compared to that cycled with PDS. The surface characteristics of the SEI layer can be regulated by selecting a suitable molecular dipole electrolyte. Utilizing asymmetrically functionalized MPS with thiol and sulfonate groups allows for compositional uniformity and structural durability of the SEI layers, thereby ensuring stable and exceptional performance even under harsh conditions for long cycling operations.

**ADVANCED
SCIENCE NEWS**

www.advancedsciencenews.com

**NANO · MICRO
small**

www.small-journal.com

2.4. Structure Characterization of Li Metal

Li metal anodes undergo substantial Li deposition and striping process under a two-digit micron scale (≈30–50 μm). This indicates that controlling the crystallinity of the reacted Li anode portion for Li deposition and stripping is a key factor in achieving a uniform and dense Li layer during cycling. Nucleation and the subsequent growth of Li predominantly determine the morphologies of the reacted Li metal surface owing to the preferential direction of Li crystal growth. To elucidate the crystalline growth mechanism of Li with different additives, we compared the crystalline structures of the discharged Li metal surface after cycling the Li–Li symmetric cells using ex situ X-ray diffraction (XRD) analysis (**Figures 5a** and **S10**, Supporting Information). The body-centered crystalline structure of Li metal had the most stable (110) surface with a high atomic density, and the dominant peak intensity of the (110) plane indicated planar and flattened growth of the Li metal surface compared to other facets such as the (200) or (211) planes associated with the dendritic growth of Li.[8a,30] After the 1st cycle, the pristine Li metal exhibited a (200) peak higher than the (110) peak. The relative ratio of the (200) plane to the (110) plane became more dominant after the 3rd and 10th cycles. For the Li growth process on pristine Li metal cycled without additives, the Li atoms diffused more rapidly on the (110) face than on the (200) face because of the higher activation energy of the (200) face associated with the unstable occupation site.[31] This effect implies that Li atoms tend to assemble more effectively in the (200) lattice, ensuring faster dendrite growth. The (110) plane was more stable than the (200) plane for Li deposition. Thus, the pristine Li metal, characterized by its elevated (200) crystal structure, is susceptible to dendrite formation. After the first cycle, the intensity of the (110) peak was significantly higher than that of the (200) peak for the Li electrode cycled with DMP. However, after the third cycle, a sharp peak corresponding to the (200) plane was observed, and this peak remained stable over the subsequent cycles. Similar to the pristine metal, the Li electrodes cycled with DMP exhibited dendritic growth with protrusion tips and did not sustain a uniform surface for an extended period. In contrast, the Li metal electrode in the presence of PDS exhibited a higher (110) peak value during the first cycle compared with the cycled Li metal anodes without additives and with DMP. This peak was maintained over repeated cycles; however, the (200) face gradually increased after the 10th cycle. Although the surface-flattening effect of PDS seemed to work smoothly at the beginning of the cycle, its effteness gradually diminished after many cycles. In contrast, the cycled Li electrodes with MPS displayed gradual crystalline conversion with a dominant (110) plane and negligible (200) plane. The Li metal structure aligned along the (110) facet was successfully maintained even after the 10th cycle. To better understand the crystalline evolution of Li metal cycled with different molecular dipole additives, the percentage of crystalline peak intensities for each Li electrode per cycle is summarized in Figure 5b. MPS molecules contribute more actively to the crystalline rearrangement of the Li metal deposit than DMP and PDS molecules and have a particularly strong influence on (110) lattice formation. These results demonstrate that MPS is the best candidate for dense and homogeneous Li deposition. Since MPS inhibits dendrite growth while maintaining a leveling effect over repeated Li deposition/stripping, it functions most effectively by fundamentally regulating the growth of protrusion tips rather than removing them.

2.5. DFT Calculation of the Additive Adsorption Energy on Li Metal Surface

We utilized the GaussView program to calculate the dipole moments of DMP, PDS, and MPS, as shown in Figure 5c. The calculation results revealed that MPS exhibited the highest value (4.7 D) among the additives (3.9 D for PDS and 3.1 D for DMP). This indicates that MPS, which has the largest dipole moment, has the strongest interaction with Li metal on the electrode surface under a high applied field. Lithium metal bears a negative charge on its surface; hence, electrolyte additives are adsorbed onto the surface of the lithium metal in a direction that exhibits a positive charge. We based our calculations on the dipole moment. The direction of the dipole moment arrow indicates a negative charge, and a longer arrow indicates a greater difference in charge. Consequently, the electrolyte additives adhered to the Li metal surface in a direction opposite to the dipole moment arrow and attracted Li ions in the direction of this arrow. Therefore, the directional adsorption behavior of the additive with Li metal can be anticipated, as illustrated in Figure 5d. Specifically, DMP and PDS, with symmetric functional groups at their ends, exhibited a dipole moment direction that extended from the center without tilting the molecule, giving them a side-on configuration when interacting with the Li metal surface. Conversely, MPS, with different functional groups at both ends, exhibited a dipole moment towards the thiol group, leading to an end-on orientation when attached to the Li metal. Therefore, MPS, which offers the highest dipole moment and a unique end-on configuration, allows superior accessibility to the Li metal surface compared to DMP and PDS.

DFT calculations were performed to investigate the role of additives in Li plating on the Li metal surfaces. First, we calculated whether each additive interacted with the Li atoms within the electrolyte. MPS and PDS preferentially bonded to the Li atom, whereas the DMP additive tended to remain separated from the Li atom (Figure S11, Supporting Information). We assumed that the low affinity of the additive for Li atoms would reduce its effect on Li deposition. These calculations suggest that DMP marginally alters the Li deposition behavior compared to MPS and PDS.

To elucidate the role of additives in the Li plating behavior on the Li metal surface, we considered the adsorption energies of the additives bonded to a Li atom in the step model,[32] which could be located on either concave or convex sites, as illustrated in Figure 5e. We measured the tendency of the homogeneous plating of Li by comparing the difference in the adsorption energies of the additives bonded with a Li atom on the concave and convex sites. We assume that adsorption on the concave site leads to the flattening deposition of Li, whereas adsorption on the convex site results in the protrusion of the Li metal. Therefore, we can assess the thermodynamic tendency of Li (in)homogeneous plating by comparing the degree of difference between the adsorption energies at the concave and convex sites.

In this study, we compared the difference between the adsorption energies of the concave and convex sites. The adsorption
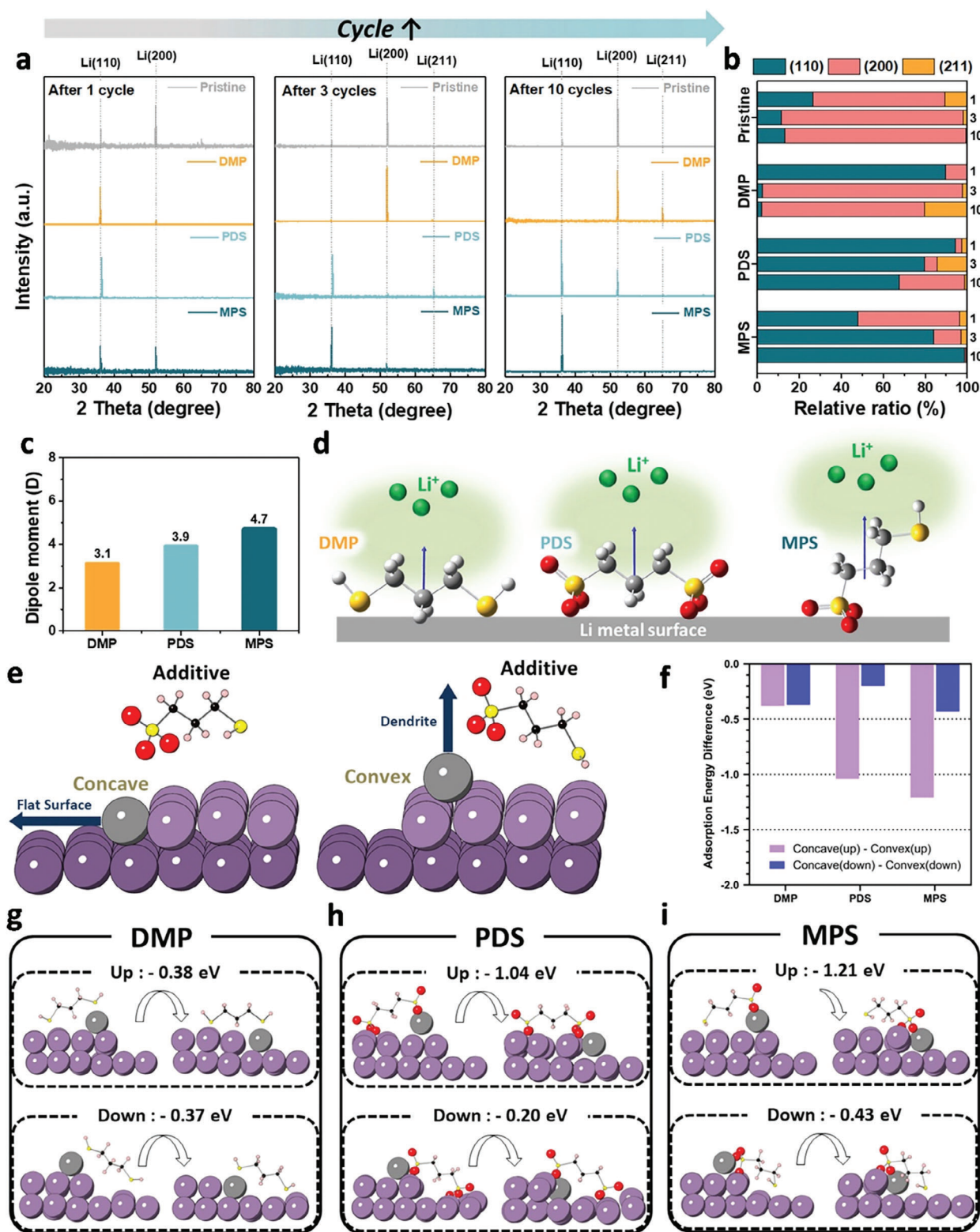
Figure 5. Ex situ XRD patterns of Li metal anodes without and with DMP, PDS, and MPS additives at different cycles: XRD of Li metal after the a) 1st cycle, 3rd cycle, 10th cycle, and b) ratio graph of each facet. c) Dipole moment magnitude graph of DMP, PDS, and MPS. Illustration of d) configurations and e) adsorption site with a slab layer: (left) concave site flattening deposition of the Li atom along with additives and (right) convex site protruding deposition of the Li atom along with additives. Difference in adsorption energy of the additive/Li atom f) on the concave and convex Li metal surfaces and g–i) on the Li metal surface depending on additive orientation along with atomic configuration: g) DMP, h) PDS, and i) MPS additives.

RIGHTS LINK

energy calculations (DMP, PDS, and MPS) indicated that a preference for Li deposition on concave sites, regardless of the orientation of the additives (Figure 5f). While Li atoms universally and energetically favor concave sites, the extent of this preference significantly varies depending on the type of additive used. We considered two different additive orientations near the step defects: up and down orientations. The "up" orientation refers to the additive being positioned on a step layer, while the "down" orientation indicates that the additive is located on an Li layer without a step layer.

Notably, MPS demonstrated the strongest thermodynamic driving force for directing a Li atom to concave sites compared to directing it to convex sites, with this tendency being quantitatively significant in both orientations of the additives, as shown in Figure 5g–i (MPS: up: −1.21 eV and down: −0.43 eV). In a comparative analysis of PDS and DMP, distinct deposition behaviors were observed. With the molecules oriented upwards, PDS demonstrated a stronger propensity for concave site deposition than DMP (Up: DMP: −0.38 eV and PDS: −1.04 eV). Conversely, in the downward orientation, this trend was reversed (Down: DMP: −0.37 eV and PDS: −0.20 eV). When we averaged the tendencies for both up and down orientations for each additive, PDS showed a stronger tendency to deposit a Li atom bond at concave sites compared to DMP (PDS: −0.62 eV and MPS: −0.38 eV). In summary, according to our preference analysis of the additives for Li atom deposition on concave and convex sites, MPS exhibited the strongest preference for concave sites, followed by DMP and PDS.

3. Conclusions

This study demonstrated the effectiveness of MPS and proposed as a new class of surface-flattening stabilizers for achieving rapid and longer-operating LMBs. The asymmetrically functionalized MPS with thiol and sulfonate groups offers the following benefits: i) surface-flattening effect against Li dendrite growth under fast operation conditions over long-term cycles, ii) crystalline rearrangement of the Li metal structure for homogeneous deposition, and iii) formation of high-quality SEI layers with durable LiF and ion-conductive Li_2S components. The MPS additives were compared with symmetrically functionalized DMP and PDS molecules with thiol and sulfonate ends, respectively. MPS facilitated over 1200 cycles at a high current density in Li–Li symmetric cells and maintained a capacity retention of 94% after 100 cycles in the $Li|V_2O_5$ full-cell test, demonstrating its superior cycling stability and durability and outperforming both DMP and PDS additives. Among the symmetric electrolyte additive molecules, PDS with a higher dipole moment exhibited better performance than DMP, which was comparable to that of MPS, demonstrating the importance of high molecular dipoles and sulfonate functional groups. Our findings are supported by experimental analyses and DFT calculations, which confirm that MPS enhances the homogeneous lithium-ion flux and promotes dense and flat lithium deposition. This stabilization was achieved through the formation of a durable and balanced SEI layer, which significantly contributed to the long lifespan and performance of the LMBs. Moreover, the preferential adsorption of MPS at defect sites minimized dendritic growth and promoted the lateral growth of crystalline Li(110), further confirming its role as

a powerful additive for future LMB technologies. Notably, MPS introduces asymmetrical sulfur-based functional groups to form conductive Li_2S within the SEI layer while maximizing the dipole moment. This research not only highlights the potential commercial applications of LMBs but also encourages the adoption of advanced electrolyte additives to optimize existing battery manufacturing processes, thus paving the way for next-generation energy storage solutions.

4. Experimental Section

Materials and Chemicals: Tetraethylene glycol dimethyl ether (TEGDME, 99%) was used as a solvent after removing water component through freshly activated 4 Å molecular sieves. A bis (trifluoromethane) sulfonimide lithium salt (LiTFSI, 99.95%) was added to the electrolyte. DMP, PDS, and MPS were used as electrolyte additives. All the materials were purchased from Sigma-Aldrich (Korea).

Preparation of the V_2O_5 Cathode Material: A lithium-free V_2O_5 cathode was synthesized using a hydrothermal procedure based on the approach developed by Zhai et al.[33] followed by heat treatment. 0.364 g of V_2O_5 powder (Sigma Aldrich, 99.6%) was mixed with 30 mL of distilled (DI) water and stirred at 40 °C. Hydrogen peroxide (5 mL) was added dropwise to the solution under continuous stirring for 30 min, followed by sonication for 30 min. Subsequently, the solution was poured into Teflon-line autoclaves and put in an oven at 200 °C for 48 h. The synthesizer was cooled in air, and an orange-colored precipitate was obtained by centrifugation, which was washed several times with ethanol and distilled (DI) water. It was then dried in an oven at 70 °C for 8 h. The cathode was prepared by mixing an active material (70 wt%), carbon black (Super-P Li) (20 wt%), and poly(vinylidene fluoride) (PVDF) (10 wt%) dissolved in N-methyl −2-pyrrolidone (NMP). The slurry was evenly cast on an Al foil and vacuum-dried at 70 °C for 8 h.

Preparation of Li–Li Symmetric Cells: The Li–Li cell test was conducted using R2032 coin-type cells (Wellcos Corp.), which were assembled in an argon-filled glove box. Each cell consisted of an Li foil (diameter: 12 mm) and a separator (Celgard 2500 polypropylene). The electrolyte employed contained 1 M LiTFSI dissolved in TEGDME, to which 1 wt% DMP, PDS, or MPS was added and stirred at 50 °C for 24 h. Both PDS and MPS electrolytes were stirred for at least 20 min before use to disperse the precipitate.

Full Cell Tests: Full cell tests were conducted using a 12 mm diameter Li metal anode, 14 mm diameter V_2O_5 nanorod cathode, 90 μL electrolyte, and a Celgard 2500 polypropylene separator. The base electrolyte was 1 M LiTFSI in TEGDME without and with 0.1 wt% DMP, PDS, or MPS. All full cells were cycled in a voltage range of 2.05–4.0 V versus Li/Li+.

Electrochemical Measurements: Electrochemical measurements were conducted with Li–Li symmetric cells at room temperature. The charge–discharge process was performed using a battery cycler (WBCS3000S battery test system; WonATech). EIS measurements were conducted from 1 MHz to 0.01 Hz at an amplitude of 5 mV.

Ex Situ Characterization: The crystal structures of the Li electrodes were characterized by X-ray diffraction (XRD; D8 Advance, Bruker) using a Cu-Kα source ($\lambda = 1.54$ Å). The surface morphologies of the Li-metal electrodes and V_2O_5 materials were studied using field-emission scanning electron microscopy (FE-SEM; JSM-7600F, JEOL) and transmission electron microscopy (TEM; JEM-2100F, Cs corrector, JEOL/CEOS). The surface roughness of the samples was observed using AFM (NX-10) in glove box. The characteristics of Li metal after cycling were investigated using X-ray photoelectron spectroscopy (XPS; K-alpha, Thermo UK).

Computational Details: DFT calculations[34] were performed using the Vienna ab initio simulation package (VASP) to investigate the behavior of additives on the Li metal surface. The core and valence electrons were described using projector-augmented wave potentials,[35] and a plane-wave basis set with a cut-off energy of 520 eV was used.[36] The generalized gradient approximation form of the electron exchange-correlation functional, formulated by Perdew-Burke-Ernzerhof, was employed.[37] An Γ-point cen-

**ADVANCED
SCIENCE NEWS**

www.advancedsciencenews.com

**NANO · MICRO
small**

www.small-journal.com

tered k-point mesh of $2 \times 2 \times 1$ was used. An electronic convergence criterion of 10^{-4} eV was used for all calculations.

To model the Li metal surface with defect, the (1 1 0) surface of a Li body centered cubic (BCC) structure[38] was built up with five layers, measuring 10.32 and 24.32 Å in the x- and y-direction, respectively, with a vacuum region of 27 Å in the z-direction. Each layer consisted of 30 Li atoms. In addition, a step layer was constructed by covering half of the surface, which consists of 15 Li atoms from the top layer. For all calculations, the bottom two layers of Li were fixed to their bulk position, and the simulation cell was relaxed to an atomic force tolerance of 0.05 eV/Å. The adsorption energy of additives binding with a Li atom was calculated as

$$\Delta E_{ads} = \Delta E_{surface + additive} - \Delta E_{surface} - \Delta E_{additive} \qquad (1)$$

where $\Delta E_{surface + additive}$ is the total energy of the surface model with additive, $\Delta E_{surface}$ is the total energy of the isolated Li surface, and $\Delta E_{additive}$ is the energy of the additive binding to an Li atom in the bulk.

Supporting Information

Supporting Information is available from the Wiley Online Library or from the author.

Conflict of Interest

The authors declare no conflict of interest.

Data Availability Statement

The data that support the findings of this study are available from the corresponding author upon reasonable request.

[1] a) D. Deng, *Energy Sci. Eng.* **2015**, *3*, 385; b) M. Armand, J.-M. Tarascon, *Nature.* **2008**, *451*, 652; c) Y. J. Choi, Y. J. Kim, S. Kim, G. Y. Kim, W.-H. Ryu, *Appl. Surf. Sci.* **2023**, *629*, 157444.

[2] a) B. Dunn, H. Kamath, J.-M. Tarascon, *Science.* **2011**, *334*, 928; b) B. Diouf, R. Pode, *Renewable Energy.* **2015**, *76*, 375; c) S. Cho, H. B. Son, S. Lee, S. Park, *Chem. Commun.* **2023**, *59*, 2819.

[3] a) D. Lin, Y. Liu, Y. Cui, *Nat. Nanotechnol.* **2017**, *12*, 194; b) J.-M. Tarascon, M. Armand, *Nature.* **2001**, *414*, 359; c) R. Wang, W. Cui, F. Chu, F. Wu, *J. Energy Chem.* **2020**, *48*, 145; d) F. Duffner, N. Kronemeyer, J. Tübke, J. Leker, M. Winter, R. Schmuch, *Nat. Energy.* **2021**, *6*, 123; e) B. Kim, K. Shin, G. Henkelman, W.-H. Ryu, *Chem. Eng. J.* **2023**, *477*, 147141.

[4] a) X. Gao, Y.-N. Zhou, D. Han, J. Zhou, D. Zhou, W. Tang, J. B. Goodenough, *Joule.* **2020**, *4*, 1864; b) C. Fang, J. Li, M. Zhang, Y. Zhang, F. Yang, J. Z. Lee, M.-H. Lee, J. Alvarado, M. A. Schroeder, Y. Yang, *Nature.* **2019**, *572*, 511.

[5] a) C. Yan, X. B. Cheng, Y. Tian, X. Chen, X. Q. Zhang, W. J. Li, J. Q. Huang, Q. Zhang, *Adv. Mater.* **2018**, *30*, 1707629; b) F. Hai, Y. Yi, Z. Xiao, J. Guo, X. Gao, W. Chen, W. Xue, W. Hua, W. Tang, M. Li, *Adv. Energy Mater.* **2024**, *14*, 2304253.

[6] a) Z. Han, C. Zhang, Q. Lin, Y. Zhang, Y. Deng, J. Han, D. Wu, F. Kang, Q. H. Yang, W. Lv, *Small Methods.* **2021**, *5*, 2001035; b) J. Wu, Z. Rao, X. Liu, Y. Shen, C. Fang, L. Yuan, Z. Li, W. Zhang, X. Xie, Y. Huang, *Adv. Mater.* **2021**, *33*, 2007428; c) X. Lin, Y. Shen, Y. Yu, Y. Huang, *Adv. Energy Mater.* **2024**, *14*, 2303918.

[7] a) S. Niu, S.-W. Zhang, D. Li, X. Wang, X. Chen, R. Shi, N. Shen, M. Jin, X. Zhang, Q. Lian, *Chem. Eng. J.* **2022**, *429*, 132156; b) S. Park, H. J. Jin, Y. S. Yun, *Adv. Mater.* **2020**, *32*, 2002193; c) D. Y. Han, S. Kim, S. Nam, G. Lee, H. Bae, J. H. Kim, N. S. Choi, G. Song, S. Park, *Adv. Sci.* **2024**, *11*, 2402156.

[8] a) S. Y. Jun, K. Shin, J. S. Lee, S. Kim, J. Chun, W. H. Ryu, *Adv. Sci.* **2023**, *10*, 2301426; b) Y. Ma, Z. Zhou, C. Li, L. Wang, Y. Wang, X. Cheng, P. Zuo, C. Du, H. Huo, Y. Gao, *Energy Storage Mater.* **2018**, *11*, 197.

[9] a) M. Nagasaki, K. Kanamura, *ACS Appl. Energy Mater.* **2019**, *2*, 3896; b) F. Wu, Z. Wen, Z. Zhao, J. Bi, Y. Shang, Y. Liang, L. Li, N. Chen, Y. Li, R. Chen, *Energy Storage Mater.* **2021**, *38*, 447.

[10] a) S. Kim, M. Lee, S. Oh, W.-H. Ryu, *Chem. Eng. J.* **2023**, *474*, 145447; b) K. Wen, X. Tan, T. Chen, S. Chen, S. Zhang, *Energy Storage Mater.* **2020**, *32*, 55; c) C. Wang, A. Wang, L. Ren, X. Guan, D. Wang, A. Dong, C. Zhang, G. Li, J. Luo, *Adv. Funct. Mater.* **2019**, *29*, 1905940.

[11] X. He, Z. Liu, Y. Yang, Z. Wang, Y. Chen, Q. Zhang, Z. Shi, Y. Tan, X. Yue, Z. Liang, *J. Mater. Chem. A.* **2023**, *11*, 10155.

[12] A. M. Haregewoin, A. S. Wotango, B.-J. Hwang, *Energy Environ. Sci.* **2016**, *9*, 1955.

[13] C. Ma, W. Jiang, Q. Duan, D. Ning, M. Wang, J. Wang, B. Chen, H. Jiang, C. Yang, W. Wu, *Adv. Energy Mater.* **2024**, *14*, 2400202.

[14] a) L. Wang, Z. Zhou, X. Yan, F. Hou, L. Wen, W. Luo, J. Liang, S. X. Dou, *Energy Storage Mater.* **2018**, *14*, 22; b) P. M. Vereecken, R. A. Binstead, H. Deligianni, P. C. Andricacos, *IBM J. Res. Dev.* **2005**, *49*, 3.

[15] a) X. Chen, G. Xu, L. Luo, *Micro Nano Lett.* **2013**, *8*, 191; b) T. P. Moffat, L.-Y. O. Yang, *J. Electrochem. Soc.* **2010**, *157*, D228; c) H. Shen, H. C. Kim, M. Sung, T. Lim, J. J. Kim, *J. Electroanal. Chem.* **2018**, *816*, 132.

[16] Q. Wang, C. Yang, J. Yang, K. Wu, C. Hu, J. Lu, W. Liu, X. Sun, J. Qiu, H. Zhou, *Adv. Mater.* **2019**, *31*, 1903248.

[17] F. Chu, J. Liu, Z. Guan, R. Deng, L. Mei, F. Wu, *Adv. Mater.* **2023**, *35*, 2305470.

[18] S. Xu, K.-H. Chen, N. P. Dasgupta, J. B. Siegel, A. G. Stefanopoulou, *J. Electrochem. Soc.* **2019**, *166*, A3456.

[19] Y. Yue, H. Liang, *Adv. Energy Mater.* **2017**, *7*, 1602545.

[20] B.-Y. Yeh, B.-S. Jian, G.-J. Wang, W. J. Tseng, *RSC Adv.* **2017**, *7*, 49605.

[21] a) Y. L. Cheah, N. Gupta, S. S. Pramana, V. Aravindan, G. Wee, M. Srinivasan, *J. Power Sources.* **2011**, *196*, 6465; b) K. Sim, J. Kwon, S. Lee, H. Song, K. Y. Cho, S. Kim, K. Eom, *Small.* **2023**, *19*, 2205086.

[22] M. Dollé, L. Sannier, B. Beaudoin, M. Trentin, J.-M. Tarascon, *Electrochem. Solid-State Lett.* **2002**, *5*, A286.

[23] Q. Wang, B. Liu, Y. Shen, J. Wu, Z. Zhao, C. Zhong, W. Hu, *Adv. Sci.* **2021**, *8*, 2101111.

**ADVANCED
SCIENCE NEWS**

www.advancedsciencenews.com

**NANO · MICRO
small**

www.small-journal.com

[24] a) J. Tan, J. Matz, P. Dong, J. Shen, M. Ye, *Adv. Energy Mater.* **2021**, *11*, 2100046; b) Z. Ju, C. Jin, X. Cai, O. Sheng, J. Wang, J. Luo, H. Yuan, G. Lu, X. Tao, Z. Liang, *ACS Energy Lett.* **2022**, *8*, 486.

[25] J. Zheng, M. H. Engelhard, D. Mei, S. Jiao, B. J. Polzin, J.-G. Zhang, W. Xu, *Nat. Energy.* **2017**, *2*, 17012.

[26] J. Di, J. L. Yang, H. Tian, P. Ren, Y. Deng, W. Tang, W. Yan, R. Liu, J. Ma, *Adv. Funct. Mater.* **2022**, *32*, 2200474.

[27] L.-P. Hou, X.-Y. Li, C.-X. Bi, Z.-X. Chen, Z. Li, L.-L. Su, P. Shi, C.-B. Jin, B.-Q. Li, J.-Q. Huang, *J. Power Sources.* **2022**, *550*, 232144.

[28] a) X. Chen, H. R. Li, X. Shen, Q. Zhang, *Angew. Chem., Int. Ed.* **2018**, *57*, 16643; b) X. Chen, T.-Z. Hou, B. Li, C. Yan, L. Zhu, C. Guan, X.-B. Cheng, H.-J. Peng, J.-Q. Huang, Q. Zhang, *Energy Storage Mater.* **2017**, *8*, 194.

[29] D. Xiao, Q. Li, D. Luo, G. Li, H. Liu, L. Shui, S. Gourley, G. Zhou, X. Wang, Z. Chen, *Small.* **2020**, *16*, 2004688.

[30] S. Y. Jun, K. Shin, Y. Lim, S. Kim, H. Kim, C. Y. Son, W. H. Ryu, *Small Struct.* **2024**, *5*, 2300578.

[31] K. Huang, Y. Liu, H. Liu, *ACS Appl. Mater. Interfaces.* **2019**, *11*, 37239.

[32] Z. Zhang, M. G. Lagally, *Science.* **1997**, *276*, 377.

[33] T. Zhai, H. Liu, H. Li, X. Fang, M. Liao, L. Li, H. Zhou, Y. Koide, Y. Bando, D. Golberg, *Adv. Mater.* **2010**, *23*, 2547.

[34] P. Hohenberg, W. Kohn, *Phys. Rev.* **1964**, *136*, B864.

[35] G. Kresse, D. Joubert, *Phys. Rev. B.* **1999**, *59*, 1758.

[36] G. Kresse, J. Furthmüller, *Phys. Rev. B.* **1996**, *54*, 11169.

[37] J. P. Perdew, K. Burke, M. Ernzerhof, *Phys. Rev. Lett.* **1996**, *77*, 3865.

[38] J. M. Zhang, F. Ma, K. W. Xu, *Surf. Interface Anal.* **2003**, *35*, 662.